





Publication Year	2019
Acceptance in OA @INAF	2021-01-07T16:10:43Z
Title	Metallicity calibrations for diffuse ionized gas and low-ionization emission regions
Authors	Kumari, Nimisha; Maiolino, Roberto; BELFIORE, FRANCESCO MICHEL CONCETTO; Curti, Mirko
DOI	10.1093/mnras/stz366
Handle	http://hdl.handle.net/20.500.12386/29587
Journal	MONTHLY NOTICES OF THE ROYAL ASTRONOMICAL SOCIETY
Number	485

Metallicity calibrations for diffuse ionized gas and low-ionization emission regions

Nimisha Kumari ^{1,2,3★} Roberto Maiolino,^{1,2} Francesco Belfiore ⁴ and Mirko Curti^{1,2}

¹Kavli Institute for Cosmology, University of Cambridge, Cambridge CB3 0HA, UK

²Cavendish Laboratory, University of Cambridge, Cambridge CB3 0HE, UK

³Institute of Astronomy, University of Cambridge, Cambridge CB3 0HA, UK

⁴European Southern Observatory, Karl-Schwarzschild-Str 2, D-85748 Garching, Germany

Accepted 2019 January 31. Received 2019 January 25; in original form 2018 October 3

ABSTRACT

Using integral field spectroscopic data of 24 nearby spiral galaxies obtained with the Multi Unit Spectroscopic Explorer, we derive empirical calibrations to determine the metallicity of the diffuse ionized gas (DIG) and/or of the low-ionization emission region (LI(N)ER) in passive regions of galaxies. To do so, we identify a large number of H II–DIG/LIER pairs that are close enough to be chemically homogeneous, and we measure the metallicity difference of each DIG/LIER region relative to its H II region companion when applying the same strong line calibrations. The O3N2 diagnostic ($=\log\left(\frac{[\text{O III}]/\text{H}\beta}{[\text{N II}]/\text{H}\alpha}\right)$) shows a minimal offset (0.01–0.04 dex) between DIG/LIER and H II regions and little dispersion in the metallicity differences (0.05 dex), suggesting that the O3N2 metallicity calibration for H II regions can be applied to DIG/LIER regions and that, when used on poorly resolved galaxies, this diagnostic provides reliable results by suffering little from DIG contamination. We also derive second-order corrections that further reduce the scatter (0.03–0.04 dex) in the differential metallicity of H II–DIG/LIER pairs. Similarly, we explore other metallicity diagnostics such as O3S2 ($=\log\left(\frac{[\text{O III}]/\text{H}\beta + [\text{S II}]/\text{H}\alpha}{[\text{N II}]/\text{H}\alpha}\right)$) and N2S2H α ($=\log\left(\frac{[\text{N II}]/[\text{S II}]}{[\text{N II}]/\text{H}\alpha}\right) + 0.264\log\left(\frac{[\text{N II}]/\text{H}\alpha}{[\text{S II}]/\text{H}\alpha}\right)$) and provide corrections for O3S2 to measure the metallicity of DIG/LIER regions. We propose that the corrected O3N2 and O3S2 diagnostics are used to measure the gas-phase metallicity in quiescent galaxies or in quiescent regions of star-forming galaxies.

Key words: ISM: abundances – galaxies: abundances – galaxies: individual – galaxies: spiral.

1 INTRODUCTION

Knowledge of the gas-phase metallicity of galaxies is essential to study various aspects of the overall evolution of galaxies. In particular, a robust metallicity measurement within galaxies is imperative for studying the physical correlations between the gas-phase metallicity of galaxies and physical properties associated with the history of chemical enrichment of galaxies such as stellar mass (i.e. mass–metallicity relation, see e.g. Tremonti et al. 2004) and star formation rate (i.e. fundamental metallicity relation, see e.g. Mannucci et al. 2010), or to explore the abundance gradients within galaxies (see e.g. Sánchez Almeida et al. 2013; Belfiore et al. 2017). The most reliable method for measuring gas-phase metallicity is the so-called direct T_e method. This method requires the detection of auroral emission lines (e.g. $[\text{O III}]\lambda 4363$, $[\text{N II}]\lambda 5755$), which are generally weak and difficult to detect. Accurate metallicity estimates using the direct T_e method become even more

difficult in high-metallicity environments as the auroral lines are even weaker in these environments (Garnett, Kennicutt & Bresolin 2004; Kewley & Ellison 2008). Moreover, the auroral lines may also underestimate the abundances of high-metallicity (supersolar) H II regions with temperature fluctuations or gradients (Stasińska 2005).

To circumvent such problems, almost a dozen indirect methods have been devised that involve the use of relatively strong emission lines (see e.g. Aller 1942; Alloin et al. 1979; Storch-Bergmann, Calzetti & Kinney 1994; Oey & Shields 2000; Denicoló, Terlevich & Terlevich 2002; Pettini & Pagel 2004; Nagao, Maiolino & Marconi 2006; Stasińska 2006; Pérez-Montero et al. 2007; Kewley & Ellison 2008; Maiolino et al. 2008; Marino et al. 2013; Dopita et al. 2016; Curti et al. 2017; Maiolino & Mannucci 2018). These indirect (‘strong line’) metallicity diagnostics have either been calibrated empirically against direct method metallicity estimates of H II regions or theoretically using photoionization models of H II regions such as MAPPINGS (Sutherland & Dopita 1993) and CLOUDY (Ferland et al. 2013) in codes such as HII-CHEMISTRY (Pérez-Montero 2014), IZI (Blanc et al. 2015), and BOND

* E-mail: nkumari@ast.cam.ac.uk

(Vale Asari et al. 2016), which utilize grids of photoionization models. These theoretical models suffer from problems such as limitations on the geometry of H II regions, poorly constrained dust depletion, and no implementation of the clumpiness of the density distribution of gas and dust (Kewley & Ellison 2008). However, another generally overlooked problem using the indirect metallicity calibrators is that both empirical and theoretical indirect diagnostics are calibrated for H II regions and do not consider the investigation of the more diffuse component of the ionized gas, the so-called diffuse ionized gas (DIG), which dominates the observed nebular emission in several classes of galaxies, or may contaminate the emission from H II regions.

The DIG, also known as the warm ionized medium, is an important ionized gas component of the interstellar medium (ISM) in galaxies, along with the denser H II regions. It is not only found in the Milky Way (Reynolds 1984, 1990), but also in the discs and haloes of the other spiral galaxies, as well as in many quiescent galaxies (see e.g. Rossa & Dettmar 2003a,b; Oey et al. 2007; Belfiore et al. 2016). Various classification methods have been devised and used to distinguish between H II regions and DIG, or to distinguish between normal star-forming (SF) galaxies and passive quiescent galaxies. These methods are based on the classical emission line ratio diagnostic diagrams (the so-called BPT diagrams, Baldwin, Phillips & Terlevich 1981) involving [S II]/H α and [N II]/H α line ratios (see e.g. Kewley et al. 2001; Kauffmann et al. 2003; Kewley et al. 2006; Belfiore et al. 2016), equivalent width of H α (EW $_{H\alpha}$) (see e.g. Cid Fernandes et al. 2011; Belfiore et al. 2016), a combination of EW $_{H\alpha}$ and [N II]/H α line ratio (Cid Fernandes et al. 2011) or surface brightness of H α emission (see e.g. Oey et al. 2007; Sanders et al. 2017; Zhang et al. 2017). The fraction of DIG increases with a decrease in the H α surface brightness of galaxies (Oey et al. 2007; Zhang et al. 2017). As mentioned above, the emission line ratios of DIG and H II regions are remarkably different. For example, [O I] λ 6300/H α , [O II] λ 3727/H β , [N II] λ 6584/H α , and [S II] λ 6717,6731/H α are known to increase in DIG regions compared to the H II regions (see e.g. Haffner, Reynolds & Tuft 1999; Voges & Walterbos 2006; Madsen, Reynolds & Haffner 2006; Blanc et al. 2009; Zhang et al. 2017). As a consequence, in terms of classification on the BPT diagrams, the emission line ratios in DIG are nearly always consistent with low-ionization nuclear emission regions or low-ionization emission regions (LIER, when the low ionization is not concentrated in the nucleus of galaxies, Belfiore et al. 2016), but also spill into the Seyfert-like region of the BPT diagrams. Given the nearly univocal DIG–LIER association, many papers simply identify DIG through the LIER BPT classification. For this reason, in the following we will often refer interchangeably to DIG and LIER, except in a few sections where we will identify the DIG emission through the EW $_{H\alpha}$ or H α surface brightness.

DIG and LIER-like line emission in red-sequence galaxies is associated with regions where no star formation is taking place despite the available reservoir of gas, and are devoid of young stellar population (Belfiore et al. 2016). However, LIER may also appear in the central region of blue sequence or green valley galaxies where star formation is mainly taking place in their spiral discs, and is also seen in the interarm regions (Singh et al. 2013; Gomes et al. 2016; Belfiore et al. 2017).

The ionization source of DIG/LIER is not very well understood. The radiation from O and B stars that is filtered and hardened by photoelectric absorption may result in DIG (Belfiore et al. 2016). However, in early-type, elliptical, and lenticular galaxies, and also in the old component of stellar discs (e.g. in the interarm regions or

the innermost parts of some discs), the hot evolved post-asymptotic giant branch stars and white dwarfs may emit hard ionizing radiation required to produce the ionized gas (Binette et al. 1994; Stasińska et al. 2008; Singh et al. 2013). Weak active galactic nuclei (AGNs), low-mass X-ray binaries, and extreme horizontal branch stars have also been suggested to be the plausible sources of radiation resulting in DIG, though their contribution might be almost negligible (Sarzi et al. 2010; Yan & Blanton 2012; Belfiore et al. 2017). We shall also mention that LIER emission may also be associated with shocked regions, but this applies only to very active galaxies with strong winds and/or in strongly interacting systems.

Despite the ubiquity of DIG in active and quiescent galaxies, no metallicity calibrator exists for estimating the abundances in LIERs or DIG-dominated regions. However, the impact of DIG contamination on metallicity measurements has been recently studied at global and spatially resolved scales. For example, the work of Sanders et al. (2017) shows that contamination of global galaxy spectrum by DIG results in an increase in the strength of low-ionization lines and a decrease in the temperature of the low-ionization zone, hence leading to an overestimate of metallicity. Their study also shows that combining DIG contamination with flux-weighting effects may bias metallicity estimates by more than 0.3 dex. Spatially resolved observations may mitigate the effects of flux weighting. Zhang et al. (2017) used integral field spectroscopic (IFS) data from Mapping Nearby Galaxies at APO (MaNGA) survey to study the effect of DIG on metallicity measurements at kiloparsec scales. However, the resolution of MaNGA or comparable IFS surveys is still much lower than the physical scale of H II regions therefore providing only a partial solution to the problem of DIG contamination.

Yan (2018) has attempted to directly derive the metallicity in galaxies dominated by DIG/LIER emission by stacking large number of galaxy spectra from the Sloan Digital Sky Survey (SDSS) and measuring the auroral lines in these systems, hence the gas temperature and therefore the gas metallicity. However, they point out that the results are somewhat puzzling as the inferred metallicity is significantly lower than inferred from other diagnostics, such as the [N II]/[O II] ratio, sensitive to the metallicity through the secondary nitrogen enrichment. The issue seems similar to the ‘temperature problem’ found in AGNs, where the use of the auroral lines gives metallicities that are up to 2 dex lower than the extrapolation of the metallicity gradient inferred from H II regions (Dors et al. 2015). These results seem to suggest that the ‘direct’ T $_e$ method has some intrinsic problems that prevent its application to regions ionized by hard radiation.

In this paper, we aim to study the impact of DIG contamination on metallicity estimates, and also to devise metallicity calibrators applicable to DIG and to a wide variety of galaxies including quiescent galaxies, which will allow us to explore their properties in depth. We utilize publicly available IFS data of nearby spiral galaxies obtained from the Multi Unit Spectroscopic Explorer (MUSE) instrument on the Very Large Telescope to separate H II regions from the DIG-dominated regions at scales of \sim 50–100 pc. These scales are comparable to the size of H II region, which may vary between a few and a few hundred pc (Kennicutt 1984). We exploit the unprecedented spatial resolution of MUSE to select DIG and H II regions, which are sufficiently close to share the same gas-phase metallicity. In particular, we define a set of closeby H II–DIG region pairs, which are expected to share the same chemical abundances, and test the application of typical strong line metallicity calibrators on the DIG regions. The true metallicity of these regions is assumed to be that of the nearby H II region (and measured using the standard metallicity diagnostics). In this framework, we can

therefore study the biases introduced by DIG contamination on metallicities estimated with strong line indicators.

The paper is organized as follows. Section 2 describes the MUSE data set and spectral-fitting technique used in estimating fluxes in emission lines. Section 3 presents the methodology to identify the chemically homogeneous H II–DIG pairs, and metallicity calibrations used in this work. Section 4 presents the main results of the analysis, and a discussion of the biases involved in using existing metallicity calibrations, new methods to mitigate such biases, and a discussion on the applicability of the new calibrations. In Section 5, we summarize our main results.

2 THE DATA

2.1 Galaxy sample and data

We have used archival MUSE data for 24 nearby spiral galaxies observed as part of the MUSE Atlas of Discs (Erroz-Ferrer et al. 2019) guaranteed time observations program (program IDs 095.B-0532(A), 096.B-0309(A), 097.B-0165(A)). The observations of these galaxies were taken between 2014 June–August, and 2014 October–2015 September (i.e. ESO P95, P96, and P97) in the wide-field mode of the MUSE instrument. These observations were performed in variable seeing conditions resulting in a seeing full width at half-maximum = 0.5–1.2 arcsec (corrected by airmass).

Fully reduced datacubes were downloaded from the Phase 3 ESO archive. These have been reduced using the MUSE pipeline version muse-1.4 and higher (Weilbacher et al. 2012, Freudling et al. 2013), which includes removal of instrumental artefacts, astrometric calibration, sky-subtraction, wavelength calibration, and flux calibration. Each datacube covers a field of view of ~ 1 arcmin \times 1 arcmin, sampled by 0.2 arcsec per spatial pixel, leading to a total of $\sim 100\,000$ individual spectra per galaxy. The wavelength range covered for each datacube is ~ 4800 – 9300 Å with a spectral resolution of 1750 at 4650 Å to 3750 at 9300 Å.

The observed galaxies are at an average distance of ~ 24 Mpc, corresponding to a spatial sampling of 23 pc per spatial pixel (~ 0.2 arcsec) and a typical spatial resolution of ~ 50 – 100 pc. The galaxies in the sample are mostly massive Sa and Sb galaxies, with three Sc and one Sd galaxy.

2.2 Spectral fitting

We measure emission line fluxes after subtracting the stellar continuum using a customized spectral-fitting routine described in Belfiore et al. (2016). An initial Voronoi binning (Cappellari & Copin 2003) is first performed on the datacubes to optimize the S/N in the continuum. A set of simple stellar population templates from the MIUSCAT library (Ricciardelli et al. 2012; Vazdekis et al. 2012) is then used to fit the stellar continuum within each Voronoi bin using penalized pixel fitting (Cappellari & Emsellem 2004; Cappellari 2017). The best-fitting continuum within each bin is scaled to the continuum level (6000–6200 Å) in the individual spaxels making up the bin and is subtracted from the observed spectrum in each spaxel to obtain a continuum-subtracted datacube containing only the emission lines. A second Voronoi binning is then performed to optimize the S/N on the H α emission line, hence the size of Voronoi bins varies (between a single pixel to several pixels) depending on the S/N of H α flux in a given pixel. The emission line flux maps are created by fitting a Gaussian profile to each emission line of interest, [O III] $\lambda 5007$, H β , H α , [N II] $\lambda 6584$, [S II] $\lambda \lambda 6717, 6731$. An S/N cut of 5 is performed on all emission line flux maps used

before carrying out further analysis. Note that the Voronoi-binned emission line flux maps are used as such a binning scheme allows us to preserve the initial spatial resolution of high-S/N regions and also allows us to analyse the regions that had low S/N at the original sampling.

3 METHOD

3.1 Selecting H II–DIG/LIER pairs

The aim of the work is to compare the nominal gas-phase metallicity of closeby H II regions and LIER/DIG regions inferred from the classical strong-line metallicity diagnostics, in order to verify whether these diagnostics for determining metallicity in H II regions hold also for the DIG/LIER or, on the contrary require some correction factor, which can therefore be calculated. For this purpose, we define a set of closeby H II–DIG/LIER pairs, which therefore are expected to be characterized by the same level of chemical enrichment in the gas-phase of the ISM. Indeed, the ISM comprising of H II regions and DIG/LIER is chemically homogeneous at sufficiently small spatial scales because the dynamical time-scale internal to these small regions is shorter than the supernovae burst time-scale responsible for ejecting metals into the ISM, or the cooling time-scales. A few observational studies have explored azimuthal variations of the metallicity in galactic discs both using the direct T_e method (Li, Bresolin & Kennicutt 2013; Berg et al. 2015) and the strong line method (Zinchenko et al. 2016; Ho et al. 2017, 2018). Generally, the azimuthal metallicity variations are found to be very small. The strongest detected azimuthal variations are about 0.1 dex, but these are inferred through the strong line method and residual variation due to the ionization parameter that may be present (despite efforts to correct for this effect). We determined the spatial scale at which chemical homogeneity starts to become important, using the catalogue of H II regions in the nearby spiral galaxy NGC 0628 from Berg et al. (2013), which provides coordinates and metallicities of H II regions robustly derived from the direct T_e method. We estimated the metallicity difference and distances between all possible pairs of H II regions in the catalogue and found that the metallicity difference between two H II regions is less than 0.1 dex when those regions were closer than ≈ 500 pc apart. We use the distance of ≈ 500 pc or less for selecting chemically homogeneous H II–DIG/LIER pairs as described later in this section.

Selection of H II–DIG/LIER pairs requires an appropriate criterion to separate H II regions from the DIG/LIER. We experimented with four different separation criteria, which include the use of two BPT diagrams ([S II]-BPT and [N II]-BPT), surface brightness of H α ($\Sigma_{H\alpha}$) and equivalent width of H α ($EW_{H\alpha}$). Among these methods, using [S II]-BPT diagnostic diagram for separating H II region from LIER/DIG/AGN ensures cleaner separation compared to that from H α surface brightness, and is less affected by variation in N/O abundance ratio compared to using the [N II]-BPT diagnostic diagram for separating H II and DIG/LIER/AGN. Moreover, subsequent analysis shows that the separation based on [S II]-BPT diagram proves superior to all other criteria. Hence, in the following, we describe the method involving [S II]-BPT in detail, while other methods only briefly.

3.1.1 [S II]-BPT

We use the classical BPT diagram of [S II]/H α versus [O III]/H β to classify spaxels within galaxies as SF, LIER/DIG-dominated,

or exhibiting line ratios of AGN, and create spatially resolved [S II]-BPT maps of all galaxies. Fig. 1 (upper panel) shows the spatially resolved [S II]-BPT diagram of three example galaxies (NGC 1042, ESO499-G37, and PGC 3853), where blue, pink, and yellow coloured data points represent the spaxels with line ratios corresponding to H II, LIER/DIG, and Seyfert regions, respectively. The solid black curve is the theoretical maximum starburst line from Kewley et al. (2001) that is used to separate H II regions from LIER/DIG/AGN when calibrating metallicity diagnostics, while the dashed black line from Kewley et al. (2006) separates DIG from AGN. Fig. 1 (lower panel) shows the corresponding spatially resolved [S II]-BPT map of the same three sample galaxies (NGC 1042, ESO499-G37, and PGC 3853), where spaxels are colour-coded following the same scheme as in the BPT diagram in the upper panel. We use these maps as reference for pair selection. We have also included Seyfert-like regions in pair selection as these regions are seen well outside the nuclear regions and therefore are unlikely associated with an AGN, but simply LIER/DIG emission whose diagnostics are formally spilling into the Seyfert region. Moreover, we will argue that potentially the revised calibration obtained by us can potentially be extended to the Seyfert region in Section 4.4.

The procedure for selecting H II–DIG pairs and the subsequent method to create the final data set for analysis is described as follows. On the resolved [S II]-BPT map of each galaxy, SF, Seyfert, and LIER/DIG regions were populated with non-overlapping circles of 1 arcsec radius. This radius was chosen on the basis of being larger than the seeing so that chosen circles within each map are independent of each other. Next, all SF circles around a LIER/DIG/Seyfert circle within a distance of ~ 500 pc were identified, such that the distance between the centres of SF circle and LIER/DIG/Seyfert circle < 500 pc. Fig. 1 (lower panel) shows examples of pair selection in three sample galaxies (NGC 1042, ESO499-G37, and PGC 3853), where each green circle denotes LIER/DIG/Seyfert circle connected by the black lines to the red circles representing all H II regions within a distance of ~ 500 pc. The number of H II–DIG pairs is, in fact, the number of LIER/DIG/Seyfert circles connected to surrounding SF circles. The representative value of any quantity (metallicity or emission line ratios) for any circle is the average of the unique values within that circle. Within an H II–DIG pair, the average of representative values of all connected SF circles is the representative value of H II region. The whole procedure was performed automatically for each galaxy. No pairs could be identified on four galaxies in the sample (NGC 4030, NGC 4603, NGC 4980, and NGC 5334) mainly because of the irregular Voronoi bins, which could not accommodate circles.

3.1.2 [N II]-BPT

As in the case of [S II]-BPT, we use the classical BPT diagram of [N II]/H α versus [O III]/H β to distinguish between SF spaxels and those spaxels exhibiting DIG/LIER/Seyfert-like line ratios. However, we use the empirical Kauffmann line (Kauffmann et al. 2003) rather than Kewley line for such a distinction as the metallicity diagnostics (O3N2 and O3S2, see Section 3.2), which we test here, were initially calibrated for galaxies lying on the left-hand sequence defined by Kauffmann line (Curti et al. 2017). Fig. 2 (upper panel) shows the spatially resolved [N II]-BPT diagram of three sample galaxies (NGC 1042, ESO499-G37, and PGC 3853), where blue and yellow coloured data points represent the spaxels with line ratios corresponding to H II and LIER/DIG/Seyfert regions, respectively. The solid black line corresponds to the theoretical

maximum starburst line from Kewley et al. (2001), and the dashed black line corresponds to the empirical Kauffmann line. We create the spatially resolved [N II]-BPT maps for each galaxy using the corresponding BPT diagrams, which we then use to select pairs of H II regions and DIG region following exactly the same procedure as for [S II]-BPT separation and pair selection. Fig. 2 (lower panel) shows examples of resolved [N II]-BPT for three galaxies where spaxels are colour-coded following the same scheme as in the corresponding BPT diagram (upper panel), and H II–DIG pairs are also marked as the red and green circles, respectively, connected by the black lines.

3.1.3 Surface brightness of H α

We use a threshold $\log \Sigma_{H\alpha}$ of $39 \text{ erg s}^{-1} \text{ kpc}^{-2}$ adopted by Zhang et al. (2017) to distinguish between an H II region spaxel and a spaxel dominated by DIG. A spaxel with $\Sigma_{H\alpha}$ above this threshold is designated as H II region provided that it also lies on the left-hand sequence defined by the Kauffmann line on the [N II]-BPT diagram. This additional criterion of [N II]-BPT was imposed as the metallicity diagnostics to be tested here were calibrated on SF galaxies defined on the basis of Kauffmann line. A spaxel with $\Sigma_{H\alpha} < 39 \text{ erg s}^{-1} \text{ kpc}^{-2}$ is designated as DIG region. Hence, we obtain spatially resolved H II–DIG map, which is then used to select H II–DIG pairs as described in Section 3.1.1. Note that we have not applied the foreground Galactic extinction correction to the surface brightness to be consistent with Zhang et al. (2017), who defined the threshold without applying foreground extinction. Moreover, Galactic extinction is very small for our sample galaxies, with $E(B - V)$ varying between 0.006 and 0.145 (Schlafly & Finkbeiner 2011).

3.1.4 Equivalent width of H α

LIER emission in extended-LIER (eLIER) and central-LIER (cLIER) is found to be associated with low $EW_{H\alpha}$ ($< 3 \text{ \AA}$; Belfiore et al. 2016). Early-type galaxies are also known to exhibit such low $EW_{H\alpha}$ associated with ionizing radiation reprocessed from hot evolved stars (Binette et al. 1994; Stasińska et al. 2008; Cid Fernandes et al. 2011). Hence, we use a threshold $EW_{H\alpha}$ of 3 \AA to create a spatially resolved H II–DIG map, where every spaxel with $EW_{H\alpha} < 3 \text{ \AA}$ is classified as LIER/DIG and H II region otherwise. We then select the H II–DIG pairs using these resolved maps and create data set in the same manner as described for [S II]-BPT selection (see Section 3.1.1). However, we find that an H II region selected on the basis of $EW_{H\alpha}$ often does not have line ratios corresponding to those of H II region sequence on BPT diagrams. As a consequence, this selection criterion results in H II–DIG pairs both of which have line ratios corresponding to DIG/LIER/Seyfert, i.e. the region where the metallicity diagnostics are not calibrated, and therefore this prevents a proper comparison of their nominal metallicities. Hence, we do not undertake the analysis of the DIG regions based on the EW analysis any further.

3.2 H II regions metallicity diagnostics

The wavelength range of the MUSE data enables us to use three indirect metallicity calibrators, N2S2H α , O3N2, and O3S2, which will be described in the following. We anticipate that these diagnostics rely on the ratio of emission lines that are sufficiently close in wavelength space not to require any significant reddening correction.

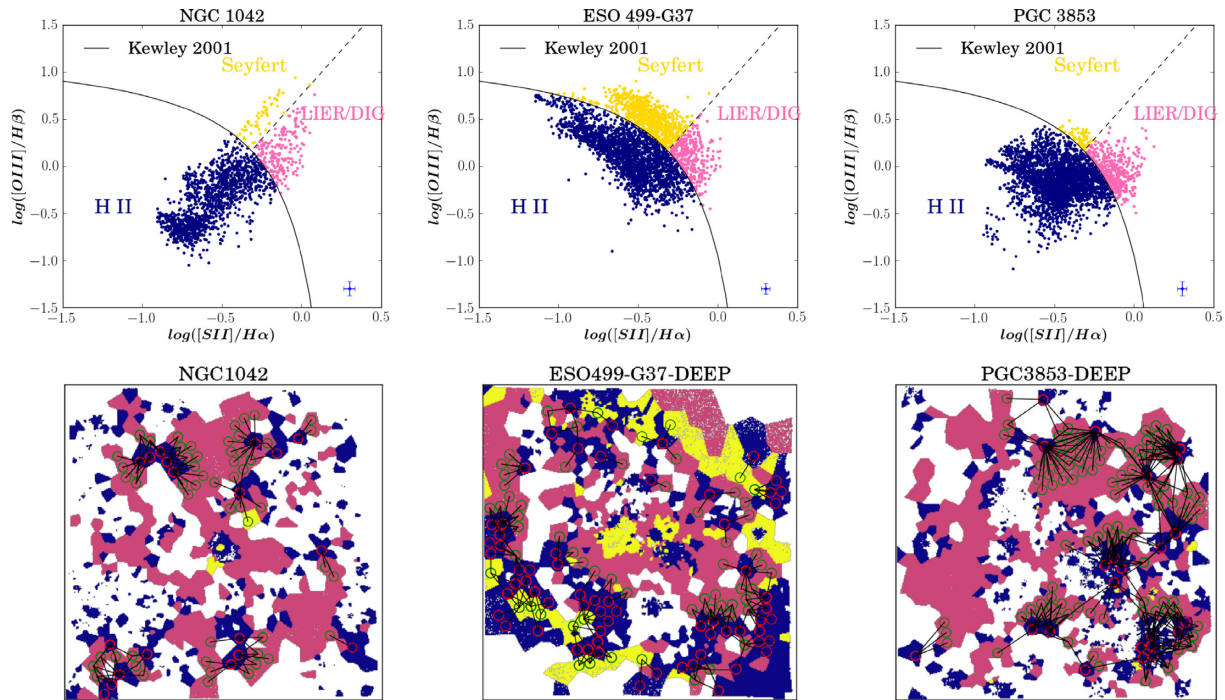


Figure 1. Emission line ratio diagnostic [S II]-BPT diagrams (upper panel) and spatially resolved [S II]-BPT maps (lower panel) of NGC 1042 (left-hand panel), ESO 499-G37 (middle panel), and PGC 3853 (right-hand panel). In all panels, blue, pink, and yellow data points denote the data points with emission line ratios corresponding to H II, LIER/DIG, and Seyfert, respectively. In the upper panel, each point corresponds to line ratios in a Voronoi bin, the black solid curve represents the theoretical maximum starburst line from Kewley et al. (2001), providing a demarcation between the bins with H II regions and DIG/LIER-dominated regions. In the DIG/LIER-dominated regime on the BPT diagnostic diagram, the dashed line shows the demarcation between the DIG/LIER and Seyfert regions from Kewley et al. 2006. The median error bars (in blue) on the emission line ratios are shown in the bottom right-hand corner. In the lower panel, the green circles denote the DIG/LIER/Seyfert circles connected by the black lines to all the red H II circles within a distance of ≈ 500 pc. The white spaxels denote the bins where emission lines have $S/N < 5$.

In the following, we define and briefly discuss these calibrators:

3.2.1 $N2S2H\alpha$

This diagnostic is defined as

$$N2S2H\alpha = \log([N II]/[S II]) + 0.264\log([N II]/H\alpha), \quad (1)$$

where $[N II] = [N II] \lambda 6584$ and $[S II] \lambda \lambda 6717, 6731$. This diagnostic has been theoretically calibrated by Dopita et al. (2016) using a grid of photoionization models implemented in MAPPINGS (Sutherland & Dopita 1993). According to their models, the gas metallicity follow a linear relation with this diagnostic in the form

$$12 + \log(O/H) = 8.77 + N2S2H\alpha \quad (2)$$

for metallicities up to $12 + \log(O/H) < 9.05$. At higher metallicity, their calibration deviates from such linear relation, and they derive the following polynomial relation that matches the theoretical models out to high metallicities:

$$12 + \log(O/H) = 8.77 + N2S2H\alpha + 0.45(N2S2H\alpha + 0.3)^5. \quad (3)$$

This diagnostic is sensitive to metallicity primarily through the $[N II]/[S II]$ and through the fact that N/S (or N/O) is observed, on average, to increase linearly with metallicity at $12 + \log(O/H) > 8$. This relationship is a crucial assumption of the model, as it provides the main sensitivity to metallicity. However, for galaxies that do not follow the assumed N/S–O/H (or equivalently N/O–O/H relation that may be an issue specifically at high redshift, see also Kumari et al. 2018), this diagnostic may provide results that are

significantly offset. The $[N II]/H\alpha$ term provides a correction for secondary dependences on ionization parameter and gas pressure. Dopita et al. (2016) claim that, as a consequence, this diagnostic is a fairly reliable metallicity tracer with only small residual dependence on other physical parameters, hence a diagnostic that can be used over a wide range of environments.

The small wavelength range required to measure all three nebular lines involved in this diagnostic makes it particularly attractive at high redshift, where optical nebular lines are shifted into the near-infrared and where instrumental limitations and atmospheric absorption make it difficult to observe broad wavelength ranges.

3.2.2 $O3N2$

This diagnostic is defined as

$$O3N2 = \log([O III]/H\beta) - \log([N II]/H\alpha), \quad (4)$$

where $[O III] = [O III] \lambda 5007$ and $[N II] = [N II] \lambda 6584$. This calibration was originally proposed by Pettini & Pagel (2004), who calibrated it empirically mostly through direct T_e measurements of H II regions. We adopt the more recent calibration obtained by Curti et al. (2017) using stacked spectra of several thousands local galaxies in the SDSS–DR7 survey. The latter calibration provides the following relation:

$$O3N2 = 0.281 - 4.765 x_{O3N2} - 2.268 x_{O3N2}^2, \quad (5)$$

where x_{O3N2} is oxygen abundance normalized to the solar value in the form $12 + \log(O/H)_{\odot} = 8.69$. This calibration has been

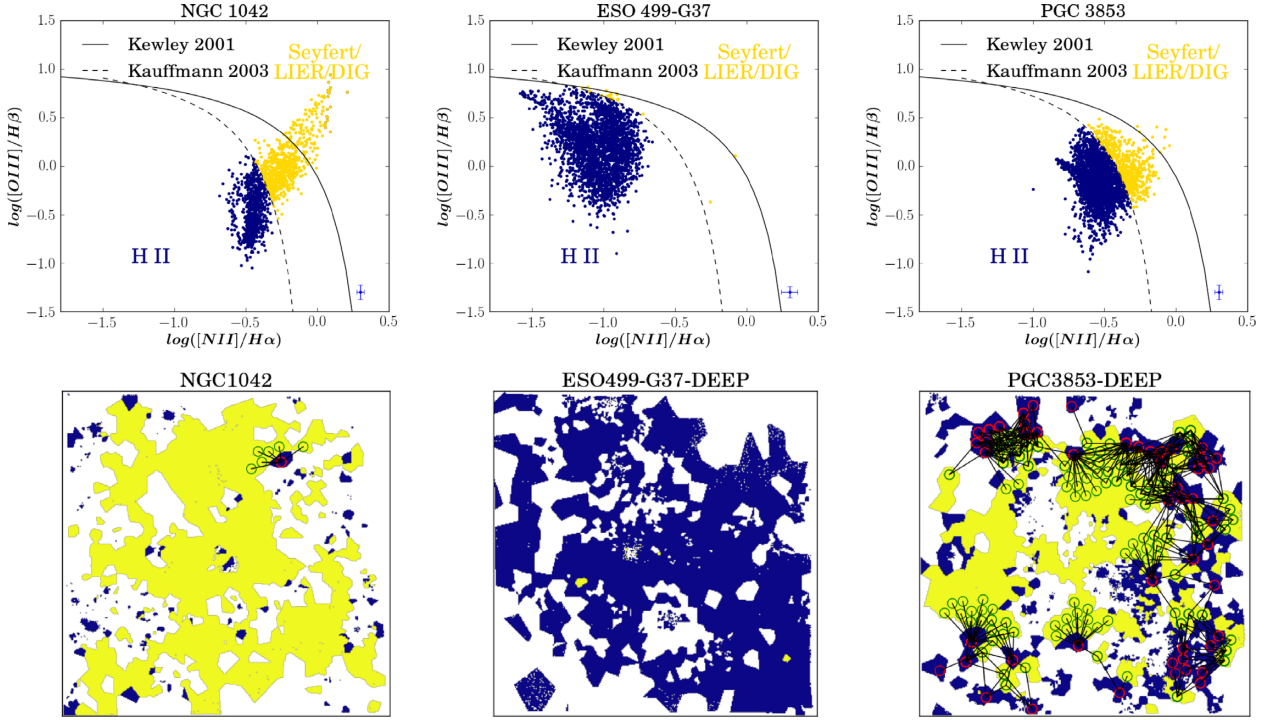


Figure 2. Emission line ratio diagnostic [N II]-BPT diagrams (upper panel) and spatially resolved [N II]-BPT maps (lower panel) of NGC 1042 (left-hand panel), ESO 499-G37 (middle panel), and PGC 3853 (right-hand panel). In all panels, the blue and yellow data points denote the data points with emission line ratios corresponding to H II, and DIG/LIER/Seyfert, respectively. In the upper panel, each point corresponds to line ratios in a Voronoi bin, the black solid curve represents the theoretical maximum starburst line from Kewley et al. (2001), while the dashed black curve represents the empirical Kauffmann line (Kauffmann et al. 2003) used here to distinguish between the bins with H II regions and DIG-dominated regions. The median error bars (in blue) on the emission line ratios are shown in the bottom right-hand corner. In the lower panel, the green circles denote the DIG/LIER/Seyfert circles connected by the black lines to all H II circles within a distance of ≈ 500 pc. A comparison of resolved BPT maps of ESO 499-G37 (bottom middle panels in Figs 1 and 2) points out that [S II]-BPT classifies this galaxy as dominated by DIG/LIER, while [N II]-BPT classifies it as dominated by red H II regions. The white spaxels denote the bins where emission lines have $S/N < 5$.

obtained in the range $7.6 < 12 + \log(O/H) < 8.85$. Of course, also this parameter is expected to be sensitive to the N/O and also to the ionization parameter.

Note that the calibrations of Curti et al. (2017) are based on stacked spectra of the central regions of galaxies (from SDSS) with relatively large projected aperture (often a few kpc), which may include both H II regions and DIG rather than individual H II regions. For robustness of our analysis, we also test the following O3N2 relation from Marino et al. (2013), which is calibrated using 3423 H II regions from the Calar Alto Legacy Integral Field Area project: $12 + \log(O/H) = 8.505 - 0.221 \text{ O3N2}$.

3.2.3 O3S2

This diagnostic is defined as

$$\text{O3S2} = \log([\text{O III}]/\text{H}\beta + [\text{S II}]/\text{H}\alpha), \quad (6)$$

where $[\text{O III}] = [\text{O III}]_{\lambda 5007}$ and $[\text{S II}] = [\text{S II}]_{\lambda\lambda 6717,6731}$. This diagnostic is very similar to the more commonly used $R_{23} = ([\text{O III}] + [\text{O II}])/\text{H}\beta$ (Pagel et al. 1979), but where the term $[\text{O II}]/\text{H}\beta$ is replaced by $[\text{S II}]/\text{H}\alpha$, and essentially exploits the fact that the [S II] flux is tightly correlated with the [O II] flux and that sulphur and oxygen are mostly produced by the same population of stars and on similar time-scales. MUSE’s wavelength range does not allow us to observe [O II] in local galaxies, while both [O III] and [S II] are observable. The additional advantage of O3S2 (relative to R_{23}) is that it is unaffected by dust reddening. The additional

advantage, relative to the other two diagnostics discussed above, is that O3S2 is not affected by variations of the N/O relative abundance.

We adopt the calibration of this diagnostic derived by Curti et al. (submitted) and is based on same data and methodology presented in Curti et al. (2017):

$$\text{O3S2} = -0.046 - 2.223 x_{\text{O3S2}} - 1.073 x_{\text{O3S2}}^2 + 0.534 x_{\text{O3S2}}^3, \quad (7)$$

where x_{O3S2} is oxygen abundance normalized to the solar value in the form $12 + \log(O/H)_{\odot} = 8.69$. The disadvantage of this diagnostic is that, like R_{23} , it is double-valued, hence it often requires another diagnostic to identify whether the metallicity is in the low- or high-metallicity branch. In the specific case of this paper, this is not an issue, as for the central regions of these local relatively massive galaxies the gas is certainly in the high-metallicity branch of the relation.

3.2.4 Other calibrators

Unfortunately, we cannot investigate and calibrate other commonly used diagnostics. We have already discussed that we cannot measure R_{23} because of MUSE’s spectral coverage. For the same reason, we cannot use the N2O2 diagnostic ($= [\text{N II}]/[\text{O II}]$, Kewley & Dopita 2002) again because [O II] is out of the spectral range. N2 ($= [\text{N II}]/\text{H}\alpha$, Pettini & Pagel 2004) has been widely adopted especially at high redshift, exploiting the narrow wavelength range needed for this diagnostic. However, it cannot be used in the

DIG/LIER range, as the N2–metallicity calibration saturates and flattens at the BPT boundary between H II regions and LIERs (see fig. 9 of Curti et al. 2017), as such it cannot be extrapolated into the LIER region.

3.3 Metallicity maps

We aim to verify if H II metallicity calibrations hold for the DIG/LIER, both within the region where these relations have been calibrated and also on their extrapolation. Hence, we use the above metallicity calibrations even beyond their range of calibration. The upper panels in Fig. 3, and in figures in the supplementary online material (Appendix A), show metallicity maps obtained using O3N2 (left-hand panel), O3S2 (middle panel), and N2S2H α (linear version, right-hand panel) of NGC 1042 and other galaxies in the sample, respectively. Metallicity maps of the same galaxy obtained from different metallicity calibrators show no apparent correlation, which points towards the inherent discrepancies between the strong line metallicity calibrators. Galaxies such as NGC 1483, NGC 4592, NGC 4980, and ESO 499-G37 (see supplementary online material Appendix A) show a much lower metallicity when estimated from N2S2H α with respect to O3S2 or O3N2. The theoretical metallicity diagnostics are known to predict higher metallicities compared to those derived from the direct T_e method (see e.g. Kewley & Ellison 2008; Kumari, James & Irwin 2017; Maiolino & Mannucci 2018). Given that O3N2 and O3S2 diagnostics here are calibrated for a sample whose metallicities are determined from direct T_e methods, we expect that the metallicities estimated from the theoretical N2S2H α calibration are higher than the O3N2 or O3S2 diagnostics. The unexpected behaviour seen in these galaxies may be due to the following reasons: First, these galaxies may have relatively lower nitrogen content than sulphur, which results in an underestimate of metallicity due to the use of [N II]/[S II] line ratio in N2S2H α diagnostic. Secondly, it is also possible that the assumption of an inherent relation between N/O and O/H in N2S2H α calibration is not valid at spatially resolved scale within these particular galaxies. For example, Kumari et al. (2018) found an unusual negative N/O versus O/H relation on a spaxel-by-spaxel basis in a blue compact dwarf galaxy NGC 4670. In addition, we should take into account the well-known discrepancies in metallicities obtained from different diagnostics (see e.g. Kewley & Ellison 2008), the reasons for which are yet to be understood. See Maiolino & Mannucci (2018) for a review.

4 RESULTS

4.1 Biases in metallicity estimates of DIG/LIER-dominated regions

Fig. 4 shows the distribution of the differential metallicities ($\Delta \log Z$) of the pairs of H II–DIG/LIER regions selected on the basis of [S II]–BPT (upper left-hand panel), [N II]–BPT (upper right-hand panel), and $\Sigma_{H\alpha}$ (lower panel), where metallicities are determined from the three metallicity calibrators described in Section 3.2. On each panel, mean offset and standard deviation of differential metallicities are denoted by $\overline{\Delta \log Z}$ and $\sigma(\Delta \log Z)$, respectively (which are also reported in Table 1).

Considering [S II]–BPT selected H II–DIG/LIER pairs (Fig. 4, upper left-hand panel), we find that O3N2 shows a negligible average offset and the least dispersion (0.05 dex), demonstrating that it is equally applicable to both H II regions and DIG/LIER-dominated regions. O3S2 underestimates the metallicity of the DIG/LIER by

0.11 dex with a dispersion of 0.09 dex. The distribution of $\Delta \log Z$ [N2S2H α] appears to be bimodal, with an average offset of -0.06 dex and a large dispersion of 0.12 dex. The latter refers to the linear calibration of the N2S2H α diagnostic; if using the non-linear calibration the dispersion is even larger (see Table 1).

Pairs selected from [N II]–BPT (Fig. 4, upper right-hand panel) appear to have comparable nominal metallicities when O3N2 diagnostic is used, such as the case of [S II]–BPT selected H II–DIG/LIER pairs. The distribution of differential metallicities obtained from O3S2 shows a large mean offset (-0.13) as well as a large dispersion (0.09 dex). N2S2H α , on the contrary shows negligible average offset but a large dispersion (0.15 dex).

Even for $\Sigma_{H\alpha}$ –selected H II–DIG/LIER pairs, O3N2 diagnostic appears to predict comparable metallicities (negligible mean offset) with the least dispersion. O3S2 diagnostic also shows negligible offset unlike the previous two cases, although the dispersion is still large. N2S2H α (linear calibration) produces a large mean offset accompanied by a large dispersion. The dispersion increases even further if adopting the non-linear calibration of N2S2H α .

Above analysis shows that except for O3N2, the other two diagnostics (N2S2H α and O3S2) will significantly bias metallicity maps of galaxies containing DIG/LIER irrespective of the adopted criterion to classify the DIG/LIER regions, hence they can introduce biases if DIG/LIER emission is mixed with the emission in unresolved/poor-resolution observations. O3N2 shows negligible average offset, indicating that this diagnostic is the least affected by DIG/LIER contamination, and can potentially be exploited to trace the metallicity in these regions. Results remain practically unchanged if we were to use O3N2 relation from Marino et al. (2013) calibrated on H II regions rather than the relation from Curti et al. (2017; see Table 1). Our further analysis is hence restricted to the more recent calibrations of Curti et al. (2017), though we also report the results for the Marino et al. (2013) calibration in Table 1.

However, these calibrators are also characterized by some secondary trends, as discussed in the following, which can be used to correct for the offsets and further reduce the dispersion. Figs 5 and 6 show the emission line ratio diagnostic diagrams ([O III]/H β versus [S II]/H α (upper panel) and [O III]/H β versus [N II]/H α (lower panel)) of the DIG/LIER counterpart in H II–DIG/LIER pairs selected from [S II]–BPT and [N II]–BPT criteria, respectively. It is interesting to note that the [S II]–BPT DIG/LIER selection (Fig. 5) results into a significant fraction of regions that are not consistently classified as LIER/DIG in the [N II]–BPT diagram. The inconsistency between the two BPT diagrams is an issue that has already been highlighted in the past (Pérez-Montero & Contini 2009). The [N II]–BPT selection is better in this regard by selecting in DIG/LIER regions most of which are classified as such also in the [S II]–BPT diagram. In both figures, data points in each panel are colour-coded with respect to the differential metallicity determined from O3S2 (left-hand panel), O3N2 (middle panel), and N2S2H α (right-hand panel). The colour-bar and scale of differential metallicities are fixed to be the same for all calibrators for a comparative view of biases in metallicities introduced by different calibrators. These BPT diagnostics clearly demonstrate that differential metallicities determined from O3S2 (left-hand panels in Figs 5 and 6) and O3N2 (middle panels in Figs 5 and 6) vary with respect to $\log ([O III]/H\beta)$. Instead, no clear trend is observed for the N2S2H α diagnostic (right-hand panels in Figs 5 and 6).

The origin of the trends of the DIG/LIER metallicity offsets with $\log ([O III]/H\beta)$, for the O3N2 and O3S2 diagrams, is likely associated with variation of the ionization parameter. However, it

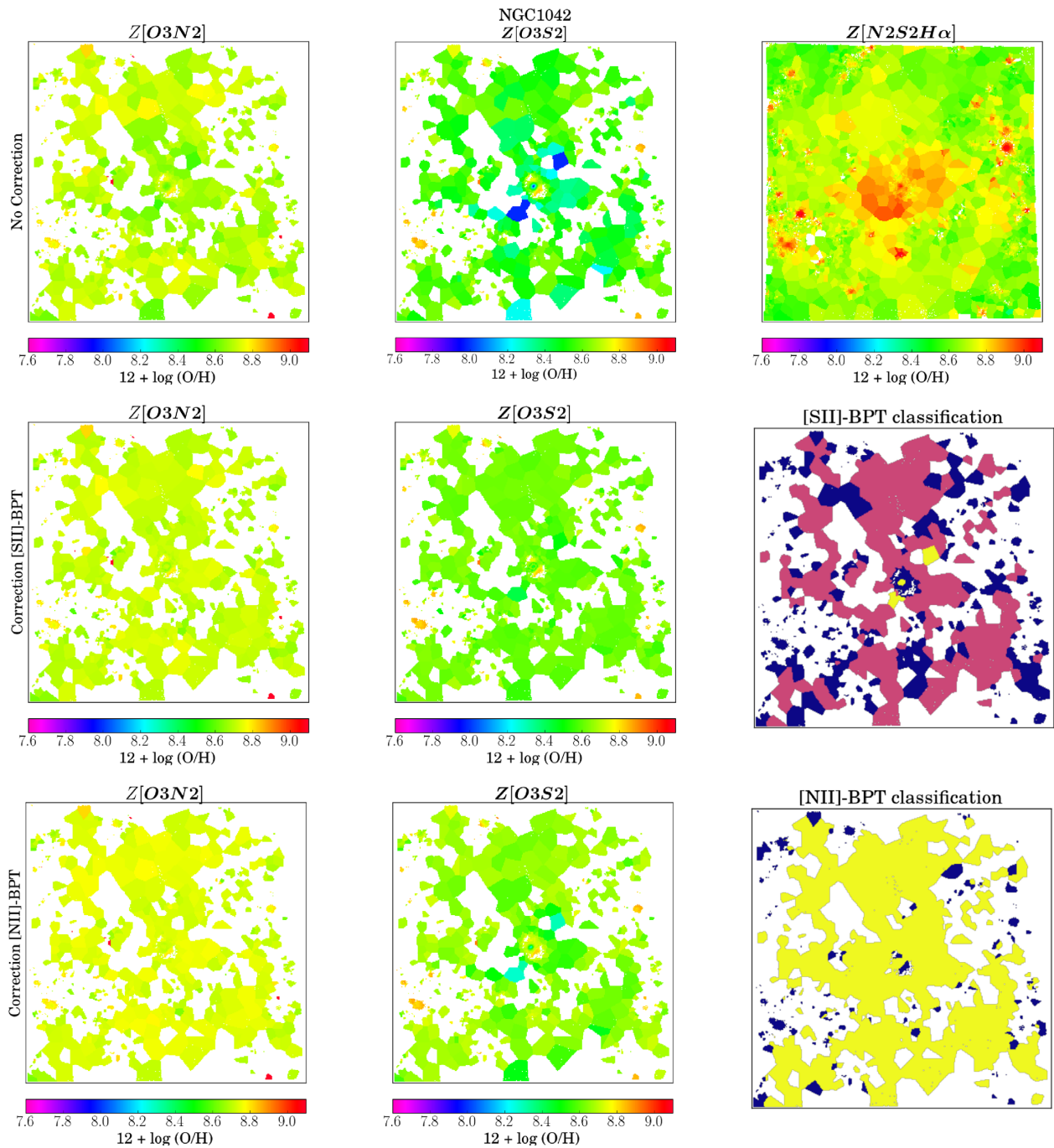


Figure 3. Upper row: Metallicity maps of NGC 1042 using original metallicity calibrators, O3N2 (left-hand panel), O3S2 (middle panel), and N2S2H α (right-hand panel). Middle-row, left-hand and central panels: Metallicity maps using O3N2 (left-hand panel) and O3S2 (middle panel), after applying the corrections obtained in Fig. 7. We also present the spatially resolved [S II]-BPT map in the middle right-hand panel to show the spaxels where metallicity corrections are applied, i.e. those spaxels with emission line ratios corresponding to DIG/LIER (pink spaxels) or Seyfert (yellow spaxels) rather than H II regions (blue spaxels). Bottom row, left-hand and central panels: Metallicity maps using O3N2 (left-hand panel) and O3S2 (middle panel), after applying the corrections obtained in Fig. 8. Bottom right-hand panel: spatially resolved [N II]-BPT to show spaxels where metallicity corrections are applied, i.e. spaxels having line ratios of Seyfert (yellow spaxels) rather than H II regions (blue spaxels). The white spaxels denote the bins with S/N of emission lines < 5 or spaxels whose emission line ratios do not permit the use of a particular metallicity calibrator.

is beyond the scope of this paper to investigate the physical origin of these correlations. Here, we mostly exploit such correlations to empirically identify calibration correction factors for the O3N2 and O3S2 diagnostics when used in the DIG/LIER region. We quantify and calibrate these trends in Figs 7 and 8. We use a least-

squares method that minimizes the scatter between the data points and the best-fitting line to fit differential metallicities from O3N2 and O3S2 with respect to $\log([\text{O III}]/\text{H}\beta)$ ratio. Fig. 7 shows the best fit for O3N2 (left-hand panel) and O3S2 (right-hand panel) for [S II]-BPT selected DIG/LIER pairs, while Fig. 8 shows the

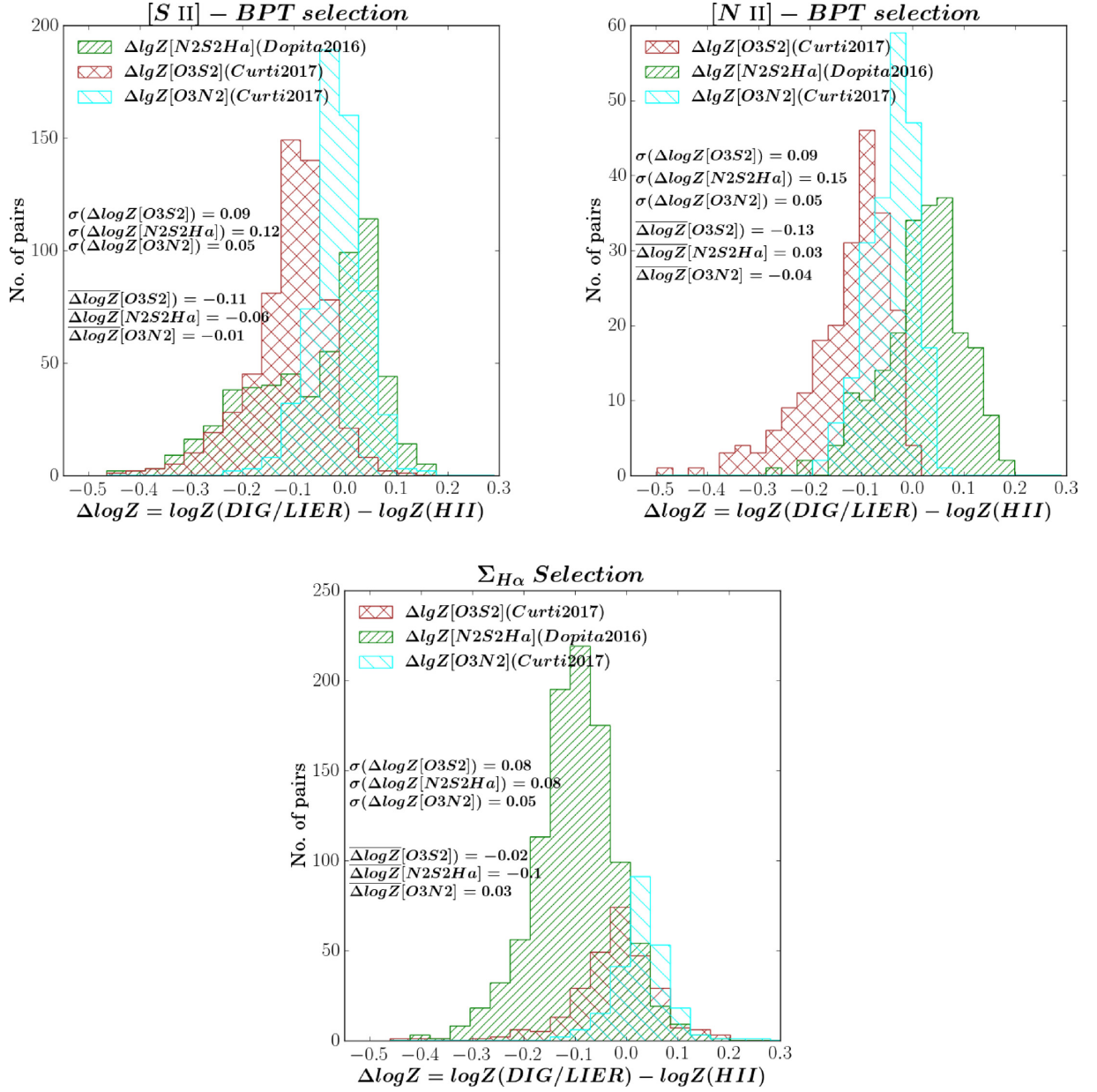


Figure 4. Distribution of differential metallicity ($\Delta \log Z$) of the H II–DIG/LIER pairs selected on the basis of the [S II]–BPT classification (upper left-hand panel), [N II]–BPT classification (upper right-hand panel), and surface brightness of H α (bottom panel). In each panel, the distribution of the differential metallicities obtained from N2S2H α , O3S2, and O3N2 are shown in the green, brown, and cyan colours, respectively. In each panel, $\overline{\Delta \log Z}$ and $\sigma(\Delta \log Z)$ are the mean and standard deviation of the distributions, respectively.

Table 1. Summary table for statistics on differential metallicities of H II–DIG/LIER pairs from different selection criteria before and after applying corrections.

Calibrator	[SII]-BPT				[NII]-BPT				$\Sigma_{\text{H}\alpha}$	
	Before		After		Before		After		Before	
	$\overline{\Delta \log Z}$	$\sigma(\Delta \log Z)$	$\overline{\Delta \log Z}$	$\sigma(\Delta \log Z)$	$\overline{\Delta \log Z}$	$\sigma(\Delta \log Z)$	$\overline{\Delta \log Z}$	$\sigma(\Delta \log Z)$	$\overline{\Delta \log Z}$	$\sigma(\Delta \log Z)$
N2S2H α (linear)	−0.06	0.12	–	–	0.03	0.15	–	–	−0.1	0.08
N2S2H α (non-linear)	−0.07	0.15	–	–	0.03	0.16	–	–	−0.1	0.09
O3N2 (Curti et al. 2017)	−0.01	0.05	−0.0002	0.04	−0.04	0.05	−0.0004	0.03	0.03	0.05
O3N2 (Marino et al. 2013)	−0.02	0.05	–	–	−0.04	0.05	–	–	0.03	0.05
O3S2	−0.11	0.09	0.006	0.05	−0.13	0.09	−0.003	0.07	−0.02	0.08

Notes: $\overline{\Delta \log Z}$ and $\sigma(\Delta \log Z)$ indicate the mean and standard deviation of differential metallicities, respectively.

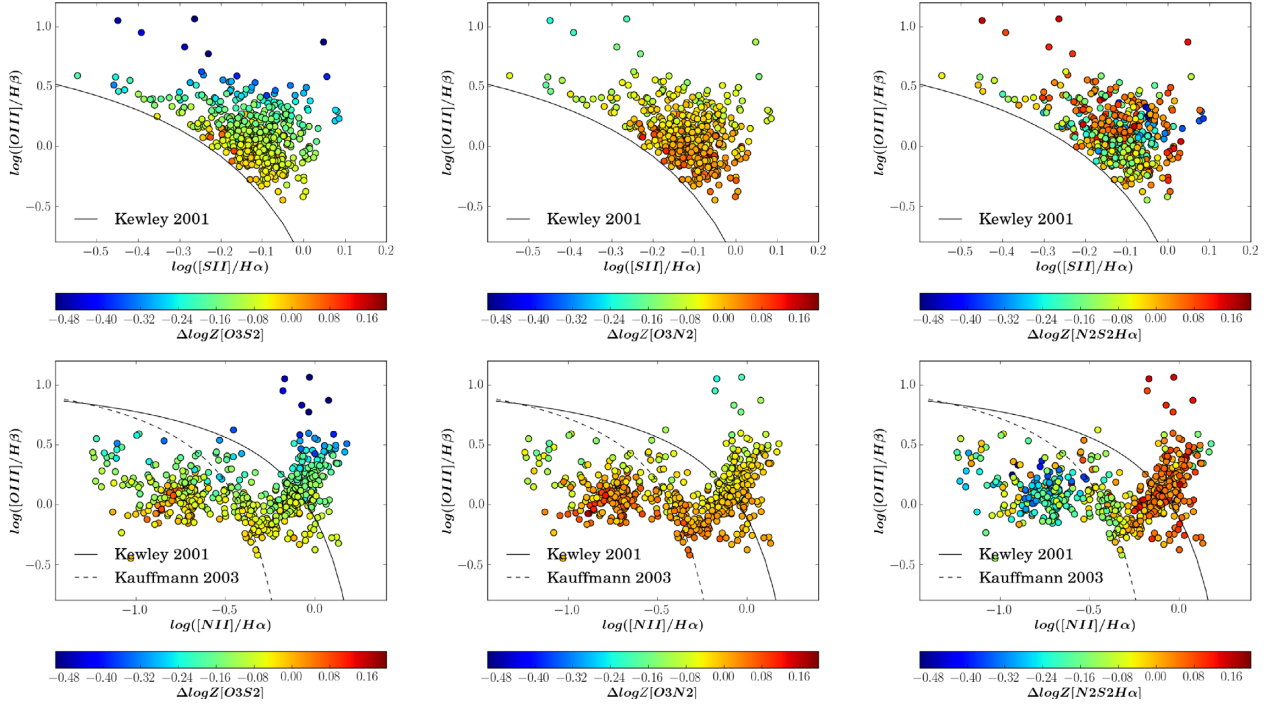


Figure 5. BPT diagnostic diagrams of the DIG/LIER counterpart in all selected pairs from [S II]-BPT selection method. The upper panel shows the $[\text{O III}]/\text{H}\beta$ versus $[\text{S II}]/\text{H}\alpha$ diagram, and the lower panel shows the $[\text{O III}]/\text{H}\beta$ versus $[\text{N II}]/\text{H}\alpha$ diagram. Here, each data point is colour-coded by the differential metallicity of the DIG/LIER component relative to the H II region counterpart. The colour-bar and scale for all panels are fixed to be the same for all panels to give a better visual comparison. Metallicities have been determined using O3S2 (left-hand panel), O3N2 (middle panel), and N2S2H α (right-hand panel) diagnostics, respectively. On all panels, the solid black line indicates the maximum starburst line from Kewley et al. (2001). On lower panel, the dashed black line indicates the demarcation line from Kauffmann et al. (2003).

best fit for O3N2 (left-hand panel) and O3S2 (right-hand panel) for [N II]-BPT selected DIG/LIER pairs. In Fig. 8 (right-hand panel), we find that the distribution of points on $\Delta\log Z - \log([\text{O III}]/\text{H}\beta)$ plane is bimodal, hence coefficients of the best-fitting line would be driven/biased by the overdensity points.

For H II-DIG/LIER pairs selected on the basis of $\Sigma_{\text{H}\alpha}$, we studied the emission line ratio diagnostic diagrams, though we did not find any trend that could be used to remedy the observed offset in the differential metallicities. As such, H II-DIG/LIER pairs selected from $\Sigma_{\text{H}\alpha}$ are not investigated any further.

4.2 New calibrations

Based on the above corrections for the O3N2 and O3S2 metallicity calibrations, we propose metallicity calibrations for the DIG/LIER regions of the form, $\log[Z(\text{DIG/LIER})_{\text{true}}] = \log[Z(\text{DIG/LIER})_{\text{orig}}] - \Delta\log(Z)$, on the basis of the best fits to differential metallicity versus $\log([\text{O III}]/\text{H}\beta)$. In the proposed form, $\log Z(\text{DIG/LIER})_{\text{true}}$ and $\log Z(\text{DIG/LIER})_{\text{orig}}$ are the true metallicity and the metallicity obtained after simply applying the H II-calibrated diagnostics (Curti et al. 2017), respectively, and $\Delta\log Z$ is the correction term obtained in Figs 7 and 8. Hence, we suggest the following two sets of corrections and calibrations, where $\text{O3} = \log([\text{O III}]/\text{H}\beta)$.

4.2.1 Calibration for [S II]-BPT selected DIG/LIER regions

For data points whose emission line ratios lie beyond the theoretical Kewley line (Kewley et al. 2001) on the [S II]-BPT diagram, we first need to determine metallicity from the H II calibration given in Section 3.2 and correct by subtracting the following terms

depending on the calibration used:

$$\Delta\log(Z)_{\text{O3N2}} = -0.156 \times \text{O3}, \quad (8)$$

$$\Delta\log(Z)_{\text{O3S2}} = -0.208 \times \text{O3}^2 - 0.309 \times \text{O3} - 0.075, \quad (9)$$

Combining these with equations (5) and (7), they result into the following final calibrations:

$$12 + \log(\text{O}/\text{H})_{\text{DIG/LIER}} = x_{\text{O3N2}} + 8.69 + 0.156 \text{O3}, \quad (10)$$

$$12 + \log(\text{O}/\text{H})_{\text{DIG/LIER}} = x_{\text{O3S2}} + 8.765 + 0.309 \text{O3} + 0.208 \text{O3}^2 \quad (11)$$

where x_{O3N2} and x_{O3S2} are determined from equations (5) and (7), respectively. Fig. 3 (middle row) shows metallicity maps of NGC 1042 obtained from O3N2 (left-hand panel) and O3S2 (middle-panel) diagnostics after applying the above corrections to the DIG/LIER-dominated spaxels (i.e. those with emission line ratios above the Kewley line) shown by the yellow/pink spaxels in spatially resolved [S II]-BPT (right-hand panel). Corresponding maps of other galaxies in the sample are shown in figures in the supplementary online material (Appendix A, middle rows). The corrected metallicity maps are more uniform, especially azimuthally, than those obtained from original metallicity calibration, even for those galaxies where we could not identify any H II-DIG/LIER pairs (which include NGC 4030, NGC 4603, NGC 4980, and NGC 5334), showing the robustness of our calibration.

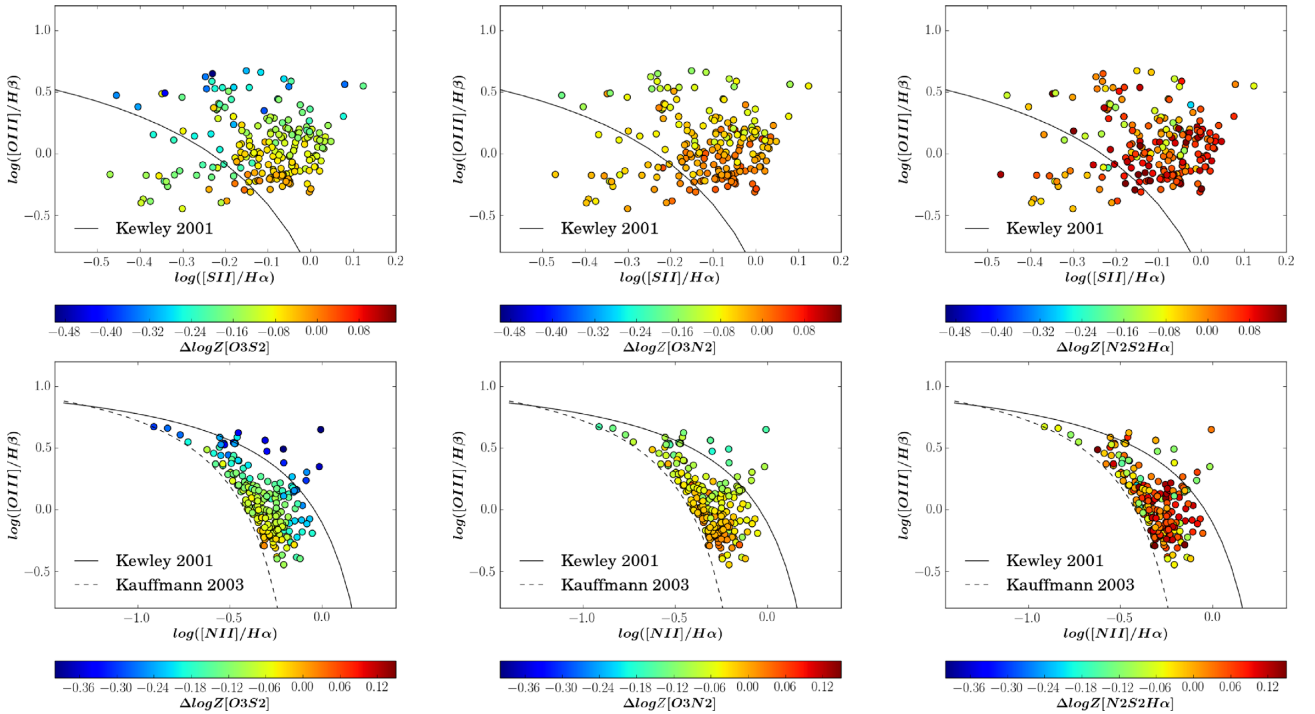


Figure 6. BPT diagnostic diagrams of the DIG/LIER counterpart in all selected pairs from [N II]-BPT selection method. The upper panel shows the [O III]/H β versus [S II]/H α diagram, and the lower panel shows the [O III]/H β versus [N II]/H α diagram. Here, each data point is colour-coded by the differential metallicity of the DIG/LIER component relative to the H II region counterpart. The colour-bar and scale for all panels are fixed to be the same for all panels to give a better visual comparison. Metallicities have been determined using O3S2 (left-hand panel), O3N2 (middle panel), and N2S2H α (right-hand panel) diagnostics, respectively. On all panels, the solid black line indicates the maximum starburst line from Kewley et al. (2001). On lower panel, the dashed black line indicates the demarcation line from Kauffmann et al. (2003).

4.2.2 Calibration for [N II]-BPT selected DIG/LIER regions

For data points whose emission line ratios lie beyond the empirical Kauffmann line (Kauffmann et al. 2003) on the [N II]-BPT diagram, we propose that the following correction terms are subtracted from the metallicity determined from H II calibration given in Section 3.2:

$$\Delta\log(Z)_{\text{O3N2}} = -0.127 \times \text{O3} - 0.033, \quad (12)$$

$$\Delta\log(Z)_{\text{O3S2}} = -0.229 \times \text{O3} - 0.113. \quad (13)$$

Combining these with equations (5) and (7), they result into the following final calibrations:

$$12 + \log(\text{O}/\text{H})_{\text{DIG/LIER}} = x_{\text{O3N2}} + 8.723 + 0.127 \text{ O3}, \quad (14)$$

$$12 + \log(\text{O}/\text{H})_{\text{DIG/LIER}} = x_{\text{O3S2}} + 8.803 + 0.229 \text{ O3}, \quad (15)$$

where x_{O3N2} and x_{O3S2} are determined from equations (5) and (7), respectively. We apply the above corrections to the DIG/LIER-dominated spaxels (i.e. those with emission line ratios beyond the Kauffmann line) to all galaxies in sample. Fig. 3 (bottom row) shows metallicity maps of NGC 1042 obtained from O3N2 (left-hand panel) and O3S2 (middle-panel) after correction, while the corresponding maps for all other galaxies are shown in figures (bottom rows) in the supplementary online material (Appendix A).

4.3 Residual differential metallicity after correction

The metallicity maps obtained using these new calibrations for the DIG/LIER regions already show an improvement, especially in terms of much reduced metallicity contrast between H II regions and nearby DIG/LIER regions. In this subsection, we quantify such improvement.

From the corrected O3N2 and O3S2 metallicity maps of each galaxy, we estimate representative values of metallicities for H II–DIG/LIER pairs using the same methodology described in Section 3.1.1, and study the distribution of differential metallicities in Fig. 9. Left-hand panel shows the distribution for [S II]-BPT selected H II–DIG/LIER pairs, while right-hand panel corresponds to [N II]-BPT selected H II–DIG/LIER pairs. By construction, mean differential metallicity is zero for each of the two metallicity diagnostic and for both samples. A comparison of dispersions before and after applying corrections can be found in Table 1.

O3N2 shows comparable metallicity dispersions for H II–DIG/LIER samples obtained from both selection criterion, i.e. 0.04 dex for [S II]-BPT selection and 0.03 dex for [N II]-BPT selection. The dispersions are smaller than the scatter in differential metallicities before applying correction (i.e. 0.05 dex).

Like O3N2, O3S2 also shows comparable metallicity dispersion for H II–DIG/LIER samples obtained from both selection criterion, i.e. 0.06 dex for [S II]-BPT selection and 0.07 dex for [N II]-BPT selection. Although the dispersions after correction are still larger than those obtained from O3N2, the improvement is significant with

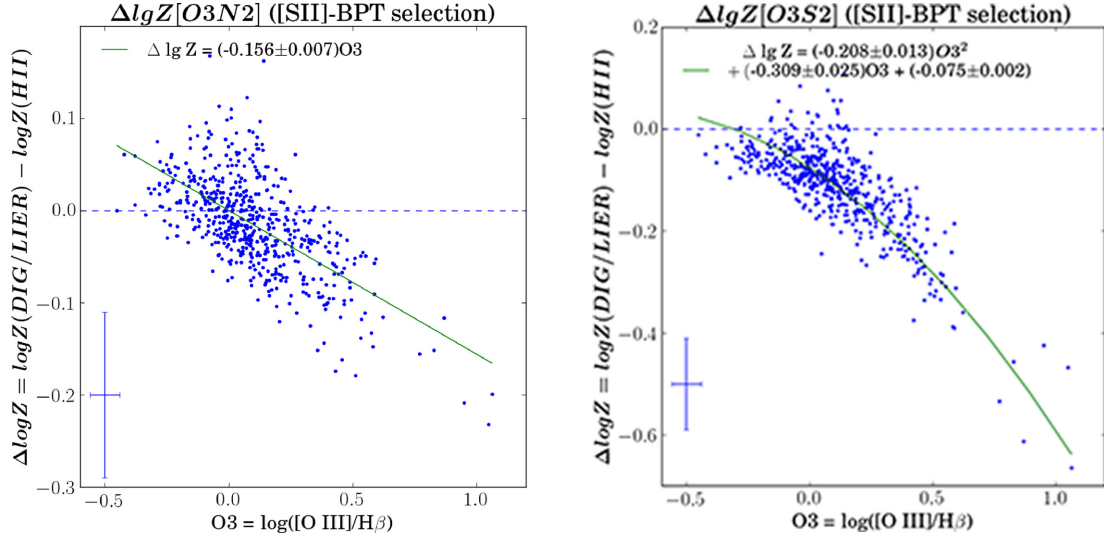


Figure 7. Least-squares best fit to differential metallicity between DIG/LIER regions and their H II-counterparts, inferred from the O3N2 (left-hand panel) and O3S2 (right-hand panel) diagnostics, versus $\log([\text{O III}]/\text{H}\beta)$. On both panels, the blue data points correspond to H II–DIG/LIER pairs from the [S II]–BPT selection, and the green line is the best fit. The blue error bars in the left-hand corner are the median uncertainties on $\log([\text{O III}]/\text{H}\beta)$ and differential metallicities. The uncertainties on $\log([\text{O III}]/\text{H}\beta)$ were obtained by propagating the uncertainties on flux measurements, whereas the uncertainties on differential metallicities included a systematic calibration uncertainty along with the measurement uncertainties. The best-fitting coefficients are shown at the top of each panel.

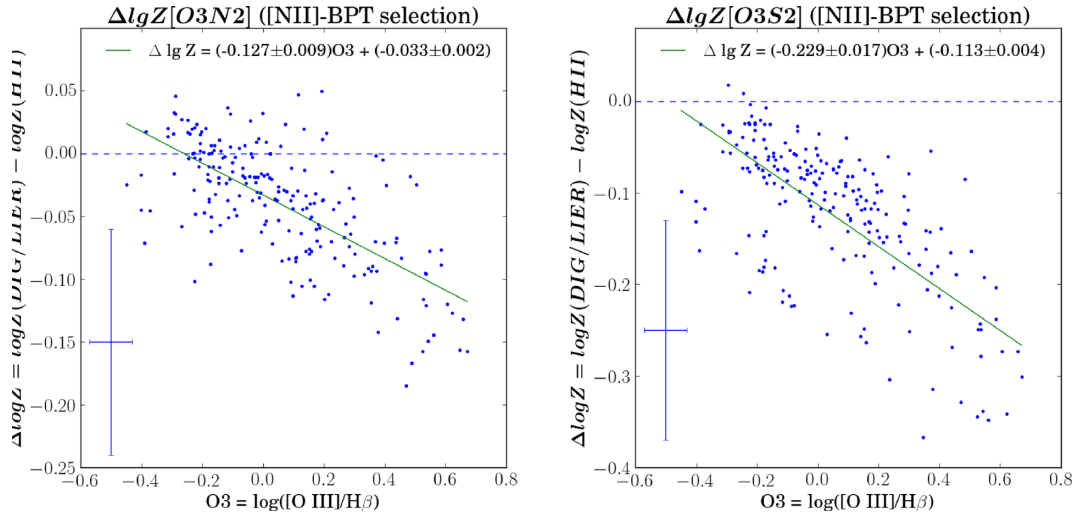


Figure 8. Least-squares best fit to differential metallicity between DIG/LIER regions and their H II-counterparts, inferred from the O3N2 (left-hand panel) and O3S2 (right-hand panel) diagnostics, versus $\log([\text{O III}]/\text{H}\beta)$. On both panels, the blue data points correspond to H II–DIG/LIER pairs from the [N II]–BPT selection, and the green line is the best fit. The blue error bars in the left-hand corner are the median uncertainties on $\log([\text{O III}]/\text{H}\beta)$ and differential metallicities. The uncertainties on $\log([\text{O III}]/\text{H}\beta)$ were obtained by propagating the uncertainties on flux measurements, whereas the uncertainties on differential metallicities included a systematic calibration uncertainty along with the measurement uncertainties. The best-fitting coefficients are shown at the top of each panel.

respect to the dispersions before the correction (0.09 dex). However, the [N II]–BPT selected pairs shows a clear bimodal distribution of differential metallicities obtained from O3S2 after correction, pointing towards the systematic biases in the correction resulting from the bimodal distribution described in Section 4.1. Hence, we recommend not to use O3S2 calibration and associated correction when DIG/LIER/Seyferts are classified using Kauffmann line.

Instead, if using [N II]–BPT we recommend using O3N2 calibration along with the associated correction.

We also point out that [S II]–BPT selected sample indicates a Gaussian distribution of differential metallicities after correction for both diagnostics (O3N2 and O3S2), which emphasizes that [S II]–BPT is a better discriminator of H II regions and DIG/LIER/Seyfert in comparison to [N II]–BPT. A comparison of O3N2 and O3S2

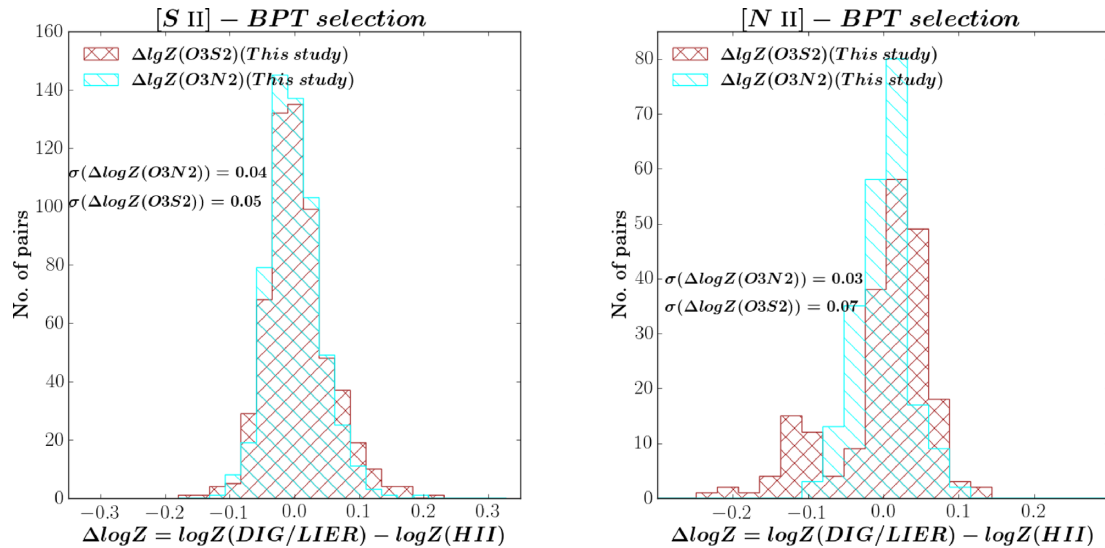


Figure 9. Distribution of corrected differential metallicity ($\Delta \log Z$) of H II-DIG/LIER pairs selected on the basis of the [S II]-BPT (left-hand panel) and [N II]-BPT (right-hand panel) diagrams. In each panel, the brown and cyan histograms represent the differential metallicity distribution from O3S2, and O3N2, respectively, after applying the correction to the DIG/LIER/Seyfert spaxels presented in Section 4.2 (equations 10, 11, 14, and 15). $\sigma(\Delta \log Z)$ denotes the standard deviation of the differential metallicity distribution. In each case, the average offsets of the distribution are zero by construction.

calibrations after corrections is presented in the supplementary material online (Appendix B).

To estimate the uncertainty on metallicity derived from our new calibrations, we must take into account the scatter in the distribution of corrected differential metallicity provided in Figure 9 and Table 1 for each calibration along with the uncertainties on the original O3N2 and O3S2 calibrations, which are of the order of 0.09 dex and 0.12 dex, respectively. For a more detailed discussion on uncertainty on original calibrations, please refer to Curti et al. 2017.

4.4 Applicability of new calibrations

The calibrations derived here have a wide range of applicability. First, since these calibrations have been derived using spatially resolved data with line ratios corresponding to DIG/LIER/Seyfert, these diagnostics will now allow us to reliably estimate the spatially resolved abundances of the ionized gas, which are not directly associated with ongoing star formation but probably to the older stellar population. Until now, studies of metallicity gradients within galaxies have not taken into account the H II and DIG components of the ISM, even though spatially resolved studies have revealed that both SF galaxies and quiescent galaxies host DIG/LIER emission extending at kpc scales (Belfiore et al. 2017). Zhang et al. (2017) show that biases introduced by DIG may be as large as the gradient in radial metallicity itself. Such biases can now be dealt with using the corrections derived in this work: either by directly using the O3N2 diagnostic (which we have shown to be the least deviating in the DIG/LIER regions) in the case of poorly resolved galaxies, or, if the DIG/LIER regions are properly resolved from the H II regions, by applying our new calibrations. By doing so, spatial correlations of metallicity and other physical properties (e.g. stellar mass surface density and star formation rate surface density) may also be studied more reliably, allowing for a deeper insight on the physics of the ISM.

Secondly, the new calibrations particularly derived from [S II]-BPT selection (equations 8 and 9) may be applied to a wide

variety of late-type and early-type galaxies as well. Using spatially resolved [S II]-BPT maps of MaNGA galaxies, Belfiore et al. (2017) established that cLIERs (characterized by LIER-like emission in the central region) are late-type galaxies lying on the transition green valley region between the main-SF-sequence and quiescent galaxies (generally with more massive bulges), while eLIERs (i.e. those with LIER-like emission extending across the entire galaxy) are similar to early-type galaxies and the passive galaxies devoid of line emission. Our new calibrations will enable to extend the metallicity scaling relations studies to these class of galaxies, whose metallicity scaling relations have been so far limited to the stellar component (e.g. Peng, Maiolino & Cochrane 2015).

Although the ionization source of DIG/LIERs is not completely understood, the most favoured scenario (at least in local normal galaxies) is that it is associated with the hard photoionizing radiation produced by evolved stellar populations (post-AGB stars), filtered and hardened UV radiation from SF regions, and weak radiatively inefficient AGNs, combined with low-ionization parameter. Even LIER-like emission associated with shocks can be included in the same category, as eventually shock ionization and excitation results from the hard emission produced by the hot gas in the post-shock gas (Allen et al. 2008). Line ratios over the LIER-Seyfert regions of the BPT diagram can therefore be generally seen as overall associated with hard ionizing radiation, with the variations of the ionization parameter being primarily responsible for the variations of the nebular line ratios in this region, together with secondary effect such as detailed shape of the ionizing radiation field, pressure, density, etc. The fact that we find that the O3N2 and O3S2 diagnostics in the DIG/LIER region show a smooth regular trend with O3, spilling well into the Seyfert regions, suggests that these diagnostics and their correction can likely be extended to the Seyfert region. Of course, this should be tested further by extending our investigation to a sample of nearby Seyfert galaxies, with ionization cones and narrow-line regions (NLR) distributed on the galactic disc (not out of the galactic plane), so that similar H II regions/Seyfert-NLR pairs can be identified to further test and/or correct/expand these metallicity calibrations.

5 SUMMARY AND CONCLUSIONS

In this paper, we utilize the IFS data of 24 nearby spiral galaxies from MUSE to study the biases in the metallicities of DIG/LIER-dominated regions when strong line calibrators N2S2H α (Dopita et al. 2016), O3N2 (Curti et al. 2017), and O3S2 (Curti et al., in preparation) are used. We define close by H II–DIG/LIER pairs that are expected to have the same metallicity, and compare their nominal metallicities using above three classical strong line metallicity diagnostics devised for H II regions. We also present suitable methods to correct the observed biases, hence providing calibrations for DIG/LIERs. Our main findings are summarized next:

(i) We separate the H II regions and DIG/LIER/Seyfert region using four different criteria: [S II]-BPT (Kewley et al. 2001), [N II]-BPT (Kauffmann et al. 2003), $\Sigma_{\text{H}\alpha}$, and EW $_{\text{H}\alpha}$. We find that BPT diagrams provide cleaner separation than threshold cuts on $\Sigma_{\text{H}\alpha}$ or on EW $_{\text{H}\alpha}$. [S II]-BPT proves to be a better discriminator than [N II]-BPT.

(ii) The original O3N2 calibration derived for H II regions appears to be the best metallicity diagnostic among the three diagnostics tested here, as the average differential metallicity predicted by O3N2 diagnostic varies by only 0.01–0.04 dex for the close by H II–DIG/Seyfert/LIER regions. Moreover, the dispersion of the differential metallicities for H II–DIG/LIER pairs is small (0.05 dex), irrespective of the method for selecting H II–DIG/LIER pairs.

(iii) The original O3S2 diagnostic is very similar to R $_{23}$ but less affected by reddening. This calibration shows large mean offsets (0.11–0.13 dex) in differential metallicities along with large dispersion (0.09 dex), for both samples of H II–DIG/LIER pairs selected from either [S II]-BPT or [N II]-BPT. However, pairs selected on the basis of $\Sigma_{\text{H}\alpha}$ show negligible mean offset but considerable scatter (0.08 dex) in the distribution of differential metallicities from O3S2.

(iv) N2S2H α diagnostic underestimates the metallicities of DIG/LIER/Seyfert by 0.06–0.1 dex compared to the close by H II region counterpart when H II–DIG/LIER pairs are selected using [S II]-BPT or $\Sigma_{\text{H}\alpha}$. No significant offset (0.03 dex) is observed in the differential metallicities of H II–DIG/LIER pairs selected from [N II]-BPT. However, dispersion is always found to be large (0.08–0.16 dex), irrespective of the selection criterion used. Unfortunately, the observed dispersion shown by N2S2H α cannot be corrected through any obvious trend.

(v) We estimate the correction offsets in O3N2 and O3S2 metallicity diagnostics as a function of [O III]/H β line ratio, i.e. $\Delta\log Z = aO3 + b$, where a and b are constants. For [S II]-BPT selected DIG/LIER/Seyferts, corrections are given by equations (8) and (9), while for [N II]-BPT selected DIG/LIER/Seyferts, corrections are given by equations (12) and (13).

(vi) After correcting the O3N2 and O3S2 derived metallicities using equations (10), (11), (14), and (15), no offset is found in differential metallicity distributions and scatters are considerably reduced. Corrected O3N2 shows dispersions of 0.04 and 0.03 dex for [S II]-BPT and [N II]-BPT selected H II–DIG/LIER pairs, respectively. Corrected O3S2 shows higher dispersions (than corrected O3N2 diagnostic), i.e. 0.05 and 0.07 dex for [S II]-BPT and [N II]-BPT selected H II–DIG/LIER pairs, respectively.

(vii) We recommend using the corrected O3N2 diagnostic (equations 10 and 14) for estimating metallicities of DIG/LIER/Seyfert-like regions, irrespective of the BPT diagram used for identifying such regions. The corrected O3S2 diagnostic is also a viable option

though it should be used only when DIG/LIER-like regions are identified using [S II]-BPT. We need to perform further experiments to confirm if these calibrations can be used for estimating metallicities of Seyfert galaxies.

The new calibrations derived in this work will allow future studies to reliably measure the spatially resolved gas-phase abundances of DIG/LIER/Seyfert-like regions in nearby SF galaxies and also gas-phase abundances of a wide variety of galaxies including early-type and passive quiescent galaxies (with nebular emission). This will enable extending the studies of chemical composition of the ISM in various types of galaxies, including the interlink between chemical abundance, star formation, and gas flows, which will further our understanding of galaxy formation and evolution.

ACKNOWLEDGEMENTS

We thank the anonymous referee for a useful and supportive report. It is a pleasure to thank Mike Irwin for discussions on multiregression analysis. NK acknowledges the financial support from the Institute of Astronomy, Cambridge, the Nehru Trust for Cambridge University during the PhD, and the Schlumberger Foundation for the post-doctoral research. RM and MC acknowledge ERC Advanced Grant 695671 ‘QUENCH’ and support by the Science and Technology Facilities Council (STFC). This research has used the NASA/IPAC Extragalactic Database (NED), which is operated by the Jet Propulsion Laboratory, California Institute of Technology, under contract with the National Aeronautics and Space Administration; SAOImage DS9, developed by Smithsonian Astrophysical Observatory; Astropy, a community-developed core PYTHON package for Astronomy (Astropy Collaboration 2013). Based on data products from observations made with ESO Telescopes at the La Silla Paranal Observatory under programme IDs 095.B-0532(A), 096.B-0309(A), and 097.B-0165(A).

REFERENCES

- Allen M. G., Groves B. A., Dopita M. A., Sutherland R. S., Kewley L. J., 2008, *ApJS*, 178, 20
- Aller L. H., 1942, *ApJ*, 95, 52
- Alloin D., Collin-Souffrin S., Joly M., Vigroux L., 1979, *A&A*, 78, 200
- Astropy Collaboration, 2013, *A&A*, 558, A33
- Baldwin J. A., Phillips M. M., Terlevich R., 1981, *PASP*, 93, 5
- Belfiore F. et al., 2016, *MNRAS*, 461, 3111
- Belfiore F. et al., 2017, *MNRAS*, 466, 2570
- Berg D. A., Skillman E. D., Garnett D. R., Croxall K. V., Marble A. R., Smith J. D., Gordon K., Kennicutt R. C., Jr., 2013, *ApJ*, 775, 128
- Berg D. A., Skillman E. D., Croxall K. V., Pogge R. W., Moustakas J., Johnson-Groh M., 2015, *ApJ*, 806, 16
- Binette L., Magris C. G., Stasińska G., Bruzual A. G., 1994, *A&A*, 292, 13
- Blanc G. A., Heiderman A., Gebhardt K., Evans N. J., II, Adams J., 2009, *ApJ*, 704, 842
- Blanc G. A., Kewley L., Vogt F. P. A., Dopita M. A., 2015, *ApJ*, 798, 99
- Cappellari M., 2017, *MNRAS*, 466, 798
- Cappellari M., Copin Y., 2003, *MNRAS*, 342, 345
- Cappellari M., Emsellem E., 2004, *PASP*, 116, 138
- Cid Fernandes R., Stasińska G., Mateus A., Vale Asari N., 2011, *MNRAS*, 413, 1687
- Curti M., Cresci G., Mannucci F., Marconi A., Maiolino R., Esposito S., 2017, *MNRAS*, 465, 1384
- Denicoló G., Terlevich R., Terlevich E., 2002, *MNRAS*, 330, 69
- Dopita M. A., Kewley L. J., Sutherland R. S., Nicholls D. C., 2016, *Ap&SS*, 361, 61
- Dors O. L., Cardaci M. V., Hägele G. F., Rodrigues I., Grebel E. K., Pilyugin L. S., Freitas-Lemes P., Krabbe A. C., 2015, *MNRAS*, 453, 4102

- Erroz-Ferrer, S. et al., 2019, *MNRAS*, preprint ([arXiv:1901.04493](https://arxiv.org/abs/1901.04493))
- Ferland G. J. et al., 2013, *Rev. Mex. Astron. Astrofis.*, 49, 137
- Freudling W., Romaniello M., Bramich D. M., Ballester P., Forchi V., García-Dabó C. E., Moehler S., Neeser M. J., 2013, *A&A*, 559, A96
- Garnett D. R., Kennicutt R. C., Jr., Bresolin F., 2004, *ApJ*, 607, L21
- Gomes J. M. et al., 2016, *A&A*, 585, A92
- Haffner L. M., Reynolds R. J., Tufté S. L., 1999, *ApJ*, 523, 223
- Ho I.-T. et al., 2017, *ApJ*, 846, 39
- Ho I.-T. et al., 2018, *A&A*, 618, A64
- Kauffmann G. et al., 2003, *MNRAS*, 346, 1055
- Kennicutt R. C., Jr., 1984, *ApJ*, 287, 116
- Kewley L. J., Dopita M. A., 2002, *ApJS*, 142, 35
- Kewley L. J., Ellison S. L., 2008, *ApJ*, 681, 1183
- Kewley L. J., Dopita M. A., Sutherland R. S., Heisler C. A., Trevena J., 2001, *ApJ*, 556, 121
- Kewley L. J., Groves B., Kauffmann G., Heckman T., 2006, *MNRAS*, 372, 961
- Kumari N., James B. L., Irwin M. J., 2017, *MNRAS*, 470, 4618
- Kumari N., James B. L., Irwin M. J., Amorín R., Pérez-Montero E., 2018, *MNRAS*, 476, 3793
- Li Y., Bresolin F., Kennicutt R. C., Jr., 2013, *ApJ*, 766, 17
- Madsen G. J., Reynolds R. J., Haffner L. M., 2006, *ApJ*, 652, 401
- Maiolino R. et al., 2008, *A&A*, 488, 463
- Maiolino R., Mannucci F., 2019, *A&ARv*, De re metallica: the cosmic chemical evolution of galaxies, 27, 3M
- Mannucci F., Cresci G., Maiolino R., Marconi A., Gnerucci A., 2010, *MNRAS*, 408, 2115
- Marino R. A. et al., 2013, *A&A*, 559, A114
- Nagao T., Maiolino R., Marconi A., 2006, *A&A*, 459, 85
- Oey M. S., Shields J. C., 2000, *ApJ*, 539, 687
- Oey M. S. et al., 2007, *ApJ*, 661, 801
- Pagel B. E. J., Edmunds M. G., Blackwell D. E., Chun M. S., Smith G., 1979, *MNRAS*, 189, 95
- Peng Y., Maiolino R., Cochrane R., 2015, *Nature*, 521, 192
- Pérez-Montero E., 2014, *MNRAS*, 441, 2663
- Pérez-Montero E., Contini T., 2009, *MNRAS*, 398, 949
- Pérez-Montero E., Hägele G. F., Contini T., Díaz Á. I., 2007, *MNRAS*, 381, 125
- Pettini M., Pagel B. E. J., 2004, *MNRAS*, 348, L59
- Reynolds R. J., 1984, *ApJ*, 282, 191
- Reynolds R. J., 1990, *ApJ*, 349, L17
- Ricciardelli E., Vazdekis A., Cenarro A. J., Falcón-Barroso J., 2012, *MNRAS*, 424, 172
- Rossa J., Dettmar R.-J., 2003a, *A&A*, 406, 493
- Rossa J., Dettmar R.-J., 2003b, *A&A*, 406, 505
- Sánchez Almeida J., Muñoz-Tuñón C., Elmegreen B. G., Méndez-Abreu J., 2013, *ApJ*, 767, 74
- Sanders R. L., Shapley A. E., Zhang K., Yan R., 2017, *ApJ*, 850, 136
- Sarzi M. et al., 2010, *MNRAS*, 402, 2187
- Schlafly E. F., Finkbeiner D. P., 2011, *ApJ*, 737, 103
- Singh R. et al., 2013, *A&A*, 558, A43
- Stasińska G., 2005, *A&A*, 434, 507
- Stasińska G., 2006, *A&A*, 454, L127
- Stasińska G. et al., 2008, *MNRAS*, 391, L29
- Storchi-Bergmann T., Calzetti D., Kinney A. L., 1994, *ApJ*, 429, 572
- Sutherland R. S., Dopita M. A., 1993, *ApJS*, 88, 253
- Tremonti C. A. et al., 2004, *ApJ*, 613, 898
- Vale Asari N., Stasińska G., Morisset C., Cid Fernandes R., 2016, *MNRAS*, 460, 1739
- Vazdekis A., Ricciardelli E., Cenarro A. J., Rivero-González J. G., Díaz-García L. A., Falcón-Barroso J., 2012, *MNRAS*, 424, 157
- Voges E. S., Waltherbos R. A. M., 2006, *ApJ*, 644, L29
- Weilbacher P. M., Streicher O., Urrutia T., Jarno A., Pécontal-Rousset A., Bacon R., Böhm P., 2012, 8451, 84510B
- Yan R., 2018, *MNRAS*, 481, 476
- Yan R., Blanton M. R., 2012, *ApJ*, 747, 61
- Zhang K. et al., 2017, *MNRAS*, 466, 3217
- Zinchenko I. A., Pilyugin L. S., Grebel E. K., Sánchez S. F., Vilchez J. M., 2016, *MNRAS*, 462, 2715

SUPPORTING INFORMATION

Supplementary data are available at *MNRAS* online.

Figures A1–A23

Figure B1

Please note: Oxford University Press is not responsible for the content or functionality of any supporting materials supplied by the authors. Any queries (other than missing material) should be directed to the corresponding author for the article.

APPENDIX A: METALLICITY MAPS OF GALAXIES BEFORE AND AFTER CORRECTION

Figs A1–A23 show the metallicity maps of 23 galaxies in the sample, before and after applying corrections. Upper panel shows the uncorrected metallicity map obtained using O3N2 (left-hand panel), O3S2 (middle panel), and N2S2H α (right-hand panel). The middle panel shows the metallicity maps obtained from O3N2 (left-hand panel) and O3S2 (right-hand panel) diagnostics after applying corrections to the DIG/LIER/Seyfert regions based on the spatially resolved [S II]-BPT map (right-hand panel). The lower panel shows the metallicity maps obtained from O3N2 (left-hand panel) and O3S2 (right-hand panel) diagnostics after applying corrections to the DIG/LIER regions based on the spatially resolved [NII]-BPT map (right-hand panel). "DEEP" at the top of some maps correspond to galaxies for which MUSE Deep 3D data cubes¹ were available.

APPENDIX B: COMPARISON OF NEW CALIBRATIONS

Fig. B1 shows a comparison of new O3N2 and O3S2 calibrations after applying corrections derived in this work based on [S II]-BPT (left-hand panel) and [NII]-BPT (right-hand panel) classifications. These data points correspond to the H II (blue) and DIG/LIER/Seyfert counterparts (green points) for all H II–DIG/LIER/Seyfert pairs.

¹www.eso.org/sci/publications/announcements/sciann17032.html

This paper has been typeset from a $\text{\TeX}/\text{\LaTeX}$ file prepared by the author.